HAL open science

Investigating Pore-Opening of Hydrogel Foams at the Scale of Freestanding Thin Films

Sébastien Andrieux, Mayur Patil, Leandro Jacomine, Aurélie Hourlier-fargette, Sascha Heitkam, Wiebke Drenckhan-Andreatta

To cite this version:

Sébastien Andrieux, Mayur Patil, Leandro Jacomine, Aurélie Hourlier-fargette, Sascha Heitkam, et al.. Investigating Pore-Opening of Hydrogel Foams at the Scale of Freestanding Thin Films. Macromolecular Rapid Communications, 2022, 43 (17), pp.2200189. 10.1002/marc.202200189 . hal-03815215

HAL Id: hal-03815215

https://hal.science/hal-03815215v1

Submitted on 14 Oct 2022

HAL is a multi-disciplinary open access archive for the deposit and dissemination of scientific research documents, whether they are published or not. The documents may come from teaching and research institutions in France or abroad, or from public or private research centers.

L'archive ouverte pluridisciplinaire **HAL**, est destinée au dépôt et à la diffusion de documents scientifiques de niveau recherche, publiés ou non, émanant des établissements d'enseignement et de recherche français ou étrangers, des laboratoires publics ou privés.

Macromolecular Rapid Communications
www.mrc-journal.de

Investigating Pore-Opening of Hydrogel Foams at the Scale of Freestanding Thin Films

Sébastien Andrieux, Mayur Patil, Leandro Jacomine, Aurélie Hourlier-Fargette, Sascha Heitkam, and Wiebke Drenckhan**

Controlling the pore connectivity of polymer foams is key for most of their applications, ranging from liquid uptake, mechanics, and acoustic/thermal insulation to tissue engineering. Despite their importance, the scientific phenomena governing the pore-opening processes remain poorly understood, requiring tedious trial-and-error procedures for property optimization. This lack of understanding is partly explained by the high complexity of the different interrelated, multiscale processes which take place as the foam transforms from an initially fluid foam into a solid foam. To progress in this field, this work takes inspiration from long-standing research on liquid foams and thin films to develop model experiments in a microfluidic "Thin Film Pressure Balance." These experiments allow the investigation of isolated thin films under well-controlled environmental conditions reproducing those arising within a foam undergoing cross-linking and drying. Using the example of alginate hydrogel films, the evolution of isolated thin films undergoing gelation and drying is correlated with the evolution of the rheological properties of the same alginate solution in bulk. The overall approach is introduced and a first set of results is presented to propose a starting point for the phenomenological description of the different types of pore-opening processes and the classification of the resulting pore-opening types.

1. Introduction

From cushioning to building, food, or biomedical industries, polymer foams are widely used lightweight materials formed by the assembly of closely-packed gas pores in a polymeric carrier matrix.[1,2] As shown in **Figure 1**a, neighboring pores can either be separated by thin films (often called "membranes" in the solid foam), leading to what is commonly called a "closed-cell foam," or they can be interconnected after rupture of the films, leading to a (partially) "open-cell foam." The percentage of interconnected pores is referred to as the "pore connectivity"[3,4] or "pore interconnectivity"[5–7] and has a crucial impact on most of the final foam properties, including liquid/gas uptake, foam mechanics, acoustic/thermal insulation, or its capacity to host bacteria and cell colonies for biomedical applications.[8–14] Despite the diversity of existing applications and the potential for innovation in key areas such as biomedicine, sustainability, and energy savings, the influence of the formulation and foaming procedure on the pore-opening process is still poorly understood. The optimization of the pore connectivity therefore relies on tedious trial-and-error procedures driven by specific industrial needs.[15] While this approach worked well over the last decades, rapid product evolution driven by environmental and innovation pressure now requires a more predictive understanding of the underlying processes.

Reasons for the current lack of predictive control of the pore-opening process in polymer foams are manyfold. Since solid foams are created by the foaming of an initially fluid-like matrix, the final pore morphology is controlled by the deformation and transport of the solidifying matrix between the pores driven by interfacial forces. The latter arise from the increasingly tight packing of the foam bubbles during the foaming process. This leads to highly complex structure/property relations in an evolving multiscale structure. Locally, the pore connectivity is controlled by the thinning and rupture of the thin films (typically 10–1000 nm thick) separating neighboring pores. The reliable description of these two interrelated processes evokes hot topics of ongoing research, including film thinning in the presence of partially mobile interfaces, polymerization/cross-linking under soft confinement or the statistics of thermally initiated hole formation in a viscoelastic thin film.[16–21] Once ruptured locally, the equilibrium of interfacial and bulk-film stresses leads to a variety of possible hole openings in-between the extreme cases of a fully open or a fully closed film. A selection of characteristic morphologies is shown in Figure 1b. Depending on the viscoelastic

S. Andrieux, M. Patil, L. Jacomine, A. Hourlier-Fargette, W. Drenckhan
Université de Strasbourg, CNRS
Institut Charles Sadron UPR22
Strasbourg F-67000, France
E-mail: sebastien.andrieux@ics-cnrs.unistra.fr; drenckhan@unistra.fr
S. Heitkam
Institute of Process Engineering and Environmental Technology
TU Dresden
Dresden 01062, Germany

The ORCID identification number(s) for the author(s) of this article can be found under https://doi.org/10.1002/marc.202200189

© 2022 The Authors. Macromolecular Rapid Communications published by Wiley-VCH GmbH. This is an open access article under the terms of the Creative Commons Attribution-NonCommercial License, which permits use, distribution and reproduction in any medium, provided the original work is properly cited and is not used for commercial purposes.

DOI: 10.1002/marc.202200189

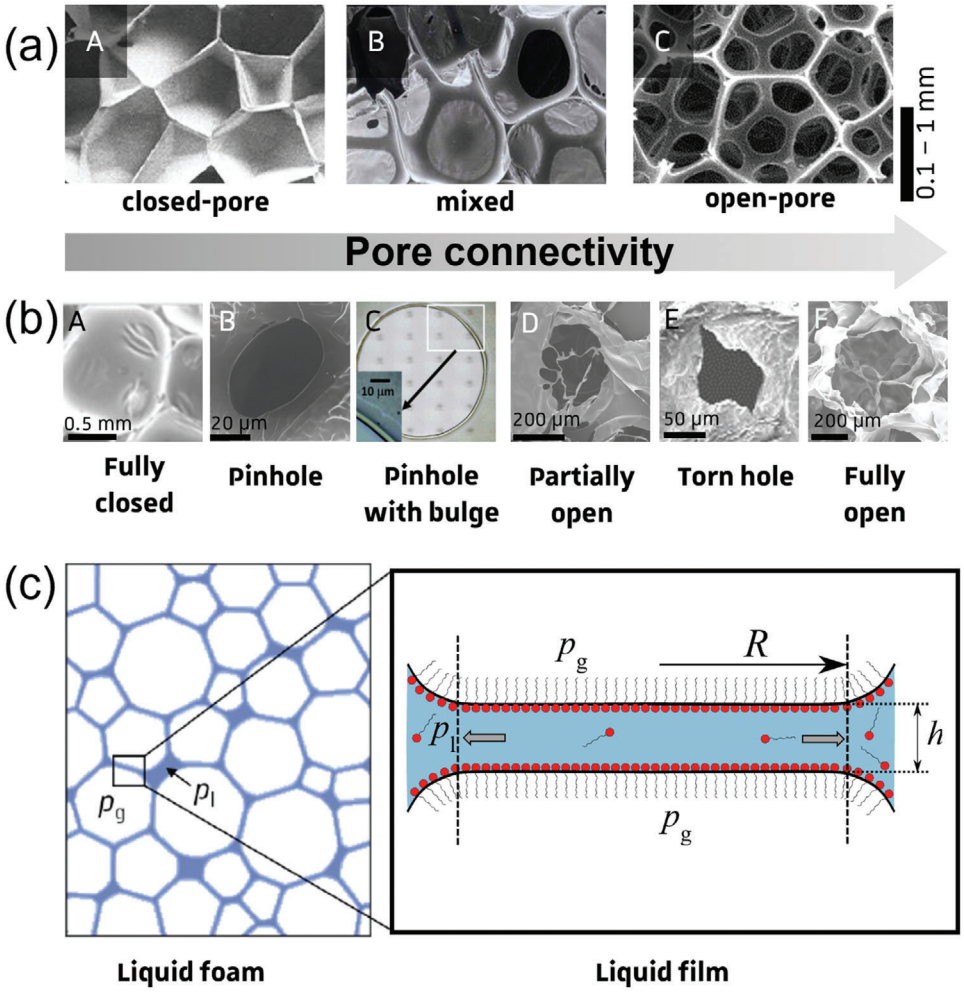

Figure 1. a) Scanning electron microscopy images of polymer foams with increasing pore connectivity: A) closed-pore polyethylene foam,[30] B) polyurethane foam (Connor Kemp), C) open-pore polyester urethane foam.[31] b) Selection of different types of pore-openings in hydrogel foams: A) Polyurethane hydrogel foam,[32] B,D–F) Freeze-dried chitosan hydrogel foams cross-linked with genipin,[33] C) Monolayer of latex bubbles.[34] c) The drainage and rupture of a foam film can be reproduced using an isolated film with the same pressure conditions. The gray arrows show liquid draining out of the film. Adapted from.[35]

state of the film and its thickness profile upon rupture, the final pore-opening may consist of round pinholes in the center or on the boundary of the film, holes may be bounded by a bulge or thick rim, they may be torn (rather than round) or partially closed with dangling material. These different scenarios indicate the complexity of the underlying processes which need to be disentangled towards a predictive understanding. It is therefore important to establish 1) a classification of the different types of pore-openings and 2) a link between the type of pore-opening, the foam formulation, the foaming process, and the overall foam morphology (pore size, density, etc.).

Isolated investigations already shed some light on cell-opening in polymer foams, whether the polymer foams originated from a liquid foam template[9,22,23] (an approach commonly called "liquid foam templating"[24–26]) or an emulsion template[3,27] (polymerized high internal phase emulsion or polyHIPE[28]). These studies show that foams with higher solid content are more likely to be closed cell. Alternatively, Andrieux et al.[29] showed that the addition of "intruders" (cellulose nanofibers in chitosan foams) could drastically reduce the pore connectivity of foams even at a constant solid content. The authors argued that the increased elasticity brought about by the cellulose nanofibers prevented the films from rupturing during solidification and drying. A more chemical approach was also investigated, as Quell et al.[3] showed that the morphology of emulsion-templated polystyrene foams and their pore connectivity can be easily modified according to whether polymerization is initiated in the continuous or the dispersed phase.

However, studying the underlying mechanisms behind pore connectivity at the scale of the foam remains a complex issue as effects driven by foam processing and foam structure are tightly interlinked with the formulation. Moreover, even though pore-opening occurs during solidification, it is virtually impossible to follow the evolution of the foam films within a 3D foam during this process with common lab-scale instruments, limiting the analysis to the morphology of the final foam.

© 2022 The Authors. Macromolecular Rapid Communications published by Wiley-VCH GmbH

To reduce some of the complexity of the underlying phenomena, we focus here on initially liquid foams whose bubbles/pores are generated by a physical (rather than chemical) foaming mechanism,[36] and which are solidified once the liquid foam has found its mechanical equilibrium structure. To investigate the evolution of the foam films, we then take inspiration from an experimental approach in liquid foam science which investigates the properties of individual foam films in dedicated "Thin Film Pressure Balances" (TFPBs).[35,37,38] In these devices, the environmental conditions of the film are controlled in a manner that reproduces those of the overall foam, as discussed in the following.

As sketched in Figure 1c, a liquid foam is characterized by its overall liquid content (or "liquid fraction") φ, its average bubble/pore size $<R>$, the liquid pressure p_l and the gas pressure p_g of the pores. If hydrostatic pressure differences are neglected, the liquid pressure p_l is constant throughout the interconnected liquid matrix. The gas pressure p_g of a pore depends on the geometry of the pore, which, in turn, is related to its size.[39,40] In a foam with modest polydispersity, one can make the hypothesis that to first approximation all gas bubbles are at the same gas pressure p_g. The difference between the gas and liquid pressure $p_c = p_g - p_l$ is then to first approximation constant and commonly called the "capillary pressure". For a foam in the low-density limit (i.e., $\varphi < 0.1$) with a surface tension γ, the capillary pressure can be estimated as[41]

$$p_c \sim \frac{\gamma}{\langle R \rangle \varphi^{1/2}} \tag{1}$$

which shows the importance of the pore size and the liquid fraction. This capillary pressure creates the main driving force which drains the continuous phase out of the films between neighboring pores. In the case of a liquid foam, this drainage proceeds until the film ruptures, or until an equilibrium is reached in the thin films, i.e., when the "disjoining pressure" created by the interaction of the stabilising agents balances the capillary pressure.[31] TFPBs are designed to create individual, free-standing horizontal films of controlled radius R at pressure conditions reproducing the capillary pressure in a foam. Since the average radius of the foam films is to first order equal to the average radius of the pores,[39,40,42] one can use Equation (1) to link the conditions in the TFPB to the properties of the low-density foam by applying the appropriate capillary pressure. More complex expressions are available in the literature to express the capillary pressure for higher liquid fractions.[41,43] Using interferometric techniques, the evolution of the thickness h of the film (Figure 1c), and its rupture, can be monitored with nanometric accuracy.

Here we use a purpose-designed microfluidic TFPB ("μTFPB") which we optimized to work with viscous liquids and with liquids that undergo solidification (Section 2.2.4).[35] This allows us to produce a film under the same pressure conditions as in the liquid foam template, and to follow its evolution during solidification. As a model system, we use alginate films which are cross-linked via calcium ions (Section 3.3). Since these foams are typically dried after (or during) cross-linking, we also dry the films in the μTFPB in a final step. The creation of holes in the μTFPB-supported film via rupture simulates the pore-opening process in the foam. It can arise at any moment during the drainage/solidification/drying process. The probability of rupture and the final hole shape depend on the formulation and the competing processes of film drainage and solidification, which can be quantified with the μTFPB.

We introduce here a first set of preliminary studies and use them to make a first suggestion of how the different scenarios and pore-opening types may be classified. For this purpose, we chose as main parameters the capillary pressure p_c and the relative time t/t_{gel} upon film formation. Here t_{gel} is the gel time of the bulk alginate solution determined using bulk shear rheology (Section 3.3). t/t_{gel} is therefore related to the viscoelastic properties of the matrix. We show that this approach allows us to propose a first phenomenological classification of pore-opening morphologies while putting in evidence some underlying general trends. Future work needs to refine the appropriate control parameters of the formulation (including the stabilizing agent) and the solidification process(es) with the goal to establish a fundamental understanding across different formulations and foaming processes.

2. Experimental Section

2.1. Materials

Calcium chloride dihydrate ($CaCl_2,2H_2O$), potassium sorbate, and δ-gluconolactone (GDL) were purchased from Sigma-Aldrich. Ethylene glycol-bis(β-aminoethyl ether)-N,N,N′,N′-tetraacetic acid (EGTA) and alginic acid sodium salt (i.e., alginate) were purchased from Alfa Aesar, USA. Sodium hydroxide (NaOH) was purchased from Merck, Germany. The surfactant Glucopon 600 CSUP (a mixture of nonionic alkyl (C_{12}-C_{14}) polyglycosides) was kindly provided by BASF, Germany. All chemicals were used as received.

2.2. Methods

2.2.1. Preparation of the Solutions

The alginate solutions were prepared based on a procedure from Sang.[44] The principle was to dissolve the calcium ions along with a chelating agent (EGTA) which bound the calcium ions at neutral pH. The alginate was then added to this solution, and gelation did not occur until the pH decreased down to ca. 4. To prepare a 0.002 M Ca-EGTA solution, 100 mL of Milli-Q water was poured into a glass bottle. Then 0.002 M of $CaCl_2,2H_2O$ and 0.02 M of EGTA were added under continuous slow stirring. To inactivate the calcium ions in the solution, a 0.1 M sodium hydroxide solution previously diluted in Milli-Q water was added to reach a stable pH of 7 ± 0.5. The solution was then transferred into a volumetric flask to reach 200 mL. To prepare the alginate solutions without $CaCl_2,2H_2O$/EGTA, 200 mL of Milli-Q water were firstly poured into a glass bottle. Then 2 wt% of alginate was added under continuous stirring using an overhead stirrer at 50 °C for 2 h.

The solutions of 0.002 M Ca-EGTA and 2 wt% alginate were the main stock solutions which were mixed in equal volumes to obtain the required concentrations (0.001 M and 1 wt%, respectively) for the film studies. The concentration of the surfactant

© 2022 The Authors. Macromolecular Rapid Communications published by Wiley-VCH GmbH

Glucopon 600 CSUP was kept constant at 0.5 wt% in all the experiments and was added to the Ca/EGTA-alginate solutions under gentle stirring to prevent the formation of bubbles. It was chosen to be well above the critical micellar concentration (CMC = 0.006 wt%, see Figure S1, Supporting Information). The solutions were kept for a maximum of two weeks.

The gelling of the alginate solutions was achieved by adding δ-gluconolactone (GDL) to acidify the solutions.[45] After adding GDL (1.25 wt%), the solution was kept under stirring for 5 min for complete mixing and then kept in an Elma Transsonic T1-H-20 ultrasonic bath for 5 min at 130 kHz to remove any bubbles formed during stirring.

2.2.2. Surface Tension Measurements

The surface tension measurements were performed using a Tracker tensiometer from Teclis. The solutions were filtered through syringe filters with a pore size of 0.2 µm. The rising bubble configuration was used except for the solution containing alginate + Ca/EGTA + surfactant, for which the pendant drop configuration was more suitable (the color of the solution and its slight turbidity did not allow for an accurate optical determination of the shape of the bubbles in the rising bubble configuration). In each case, a bubble (drop) of 8 (5) µL was generated at maximum speed and the measurement started as soon as the set volume was reached. The given error on the surface tension value was a combination of the device error (0.1×10^{-3} N m^{-1}) and the fact that equilibrium was not always fully reached during the measurement when relaxation was slow. The temperature was set to 20 °C.

2.2.3. Bulk Shear Rheology

Viscosity Measurements: Viscosity measurements were carried out using the HR20 rheometer from TA instruments at 20 °C. The cone-plate geometry was used during the study with a diameter of 60 mm, a truncation gap of 28 µm, and an angle of 1° 00 min 47 s. The cone-plate geometry allowed to have a homogeneous shear rate across the sample. The shear rates were varied from 0.1 to 1000 s^{-1}, with an acquisition time of 10 s per point. The final viscosity for each sample was taken as the zero-shear viscosity from the Cross model fitted to the data.

Gelation Kinetics: To quantify the temporal evolution of the viscoelastic properties of the gelling solutions, oscillatory rheology was carried out using a Bohlin rheometer (Gemini 150) at 20 °C. The plate-plate geometry was used during the study with a gap of 1 mm between the plate and surface at the frequency of $f = 1$ Hz ($\omega = 2\pi f$) and an amplitude of 1%. The plate-plate geometry allowed to 1) use a larger sample volume than with a cone-plate geometry, and 2) avoid any heterogeneity of the cross-linking process in the sample due to different confinements as the gap is constant across the sample. The samples were put in the rheometer while taking the precautions that there were no bubbles. Then the measurements were started approximately 20 min after the addition of GDL as described in Section 3.3. All times presented on the rheology graphs are defined with respect to the moment at which the GDL was added.

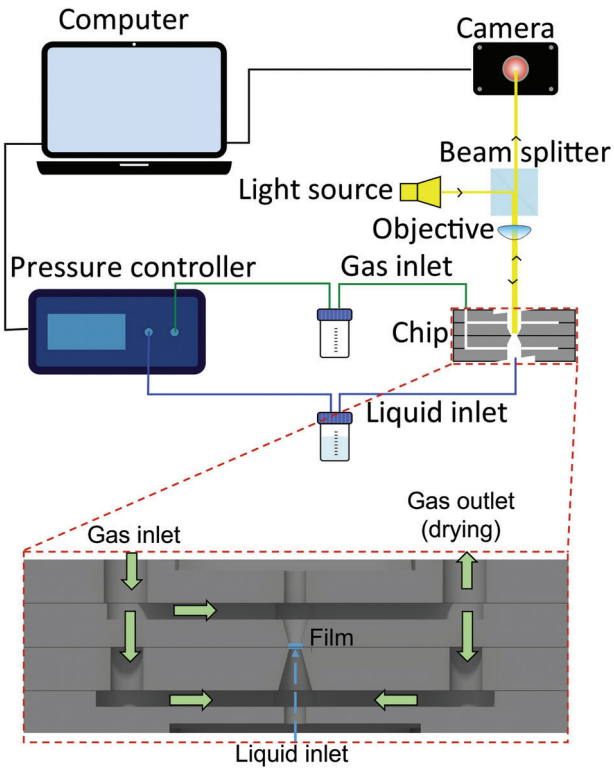

Figure 2. Schematic drawing of the microfluidic thin-film pressure balance (μTFPB). For more details see ref. [35]. The zoom shows the microfluidic chip in which the film is formed and its various inlets/outlets. Adapted from.[35]

Since we realized that the gel points showed some variation between experiments, we chose to run the rheology experiments in parallel to the film drainage experiments, as explained in Section 3.4. This allowed us to follow in real time the rheological properties of the gelling system and initiate film drainage at a known relative time t/t_{gel}.

2.2.4. Film Drainage and Rupture

A home-built microfluidic thin film pressure balance (μTFPB) was used to form stable horizontal films and to study their drainage/gelling/drying behavior. The μTFPB was thoroughly described in our previous work[35] and is schematically shown in **Figure 2**. Briefly, a microfluidic chip in which a film is formed is connected to an optical system and a pressure control set-up (Figure 2). The ELVEFLOW pressure controller OB1 Mk3 was used to independently set the gas pressure p_g and the liquid pressure p_l, which are both defined relative to the ambient pressure. The accessible pressure range of the pressure controller is 0 – 20 000 Pa and the pressure controller has an accuracy of 1 Pa. A bottle was connected between the gas outlet of the pressure controller and the gas inlet of the microfluidic chip. This bottle contained some water to provide a water-saturated atmosphere within the chip and prevent evaporation. Before each experiment, a gas pressure of 20 000 Pa was applied for 5 min, while leaving the chip slightly open to allow for humid airflow.

© 2022 The Authors. Macromolecular Rapid Communications published by Wiley-VCH GmbH

A second bottle containing the foaming solution was connected between the pressure controller and the chip. It was always ensured that the liquid level in the bottle was at the same height as the film (Figure 2) to set the hydrostatic pressure to 0 Pa (with an error of ± 2 mm, i.e., 20 Pa). A liquid pressure (typically 500 Pa) was then applied until the liquid reached the film holder (aka "bike wheel"[35,46]). The radius of the hole at the center of the bike wheel was 0.5 mm. The liquid pressure was set back to 0 Pa as soon as the hole in which the film formed was filled with liquid. The gas pressure p_g and the liquid pressure p_l were both 0 Pa and the capillary pressure p_c was thus 0 Pa as well (see Section 1). The film had then the form of a thick lens which did not drain over time. This lens was let at rest for 5 min to allow for all the surface-active species to migrate to the interface to ensure that the interface was at equilibrium (see Section 3.1.1). This also ensured that the chip was saturated with water vapor.

Film drainage was induced by applying a finite capillary pressure p_c by adjusting the gas pressure at constant liquid pressure ($p_l = 0$ Pa), i.e., the gas pressure was identical to the capillary pressure. Since the capillary pressure drives the film drainage, the liquid was expelled out of the film, as schematized by the gray arrows in Figure 1c. The time $t = 0$ s corresponds to the time at which the capillary pressure was applied. Images of the film were captured using a polychromatic 12-bit CCD camera (UEye UI-3580LE-C-HQ from iDS Imaging Development Systems GmbH). The images were generated via interferometry, which allows to relate the film color to its thickness.[37] The capillary pressure was kept constant during the entire experiment.

Once the film had drained to an equilibrium profile (i.e., one observed no evolution for 15 min), a gas outlet, closed for drainage experiments, was slightly opened to allow for a gentle airflow above and below the film for drying experiments (while the pressures set on the pressure controller were maintained). The bottle that contained water to saturate the atmosphere with water in the chip was switched with an empty bottle so that the air flowing around the film was dry. Note that since the pressure was controlled by a pressure controller, the gas flow rate in the drying experiment was not controlled quantitatively. The influence of the drying rate on the morphology of gelled films will be the scope of a future study. The drying time $t = 0$ min was taken at the time at which the gas outlet was opened. To prevent the film from being replenished by the liquid in the microfluidic channels upon drying (via osmotic effects), the liquid inlet was disconnected from the chip as soon as the gas inlet was opened.

Film Thickness via Colorimetric Mapping: To be able to estimate the thickness of the thin films, a colorimetric map was generated using a MatLab code based on Fresnel optics: the spectrum of reflected light intensity can be derived from Fresnel equations for reflection and transmission. For zero inclination angle, the reflected intensity I_r and transmitted intensity I_t are given by

$$I_r = \left(\frac{n_1 - n_2}{n_1 + n_2}\right)^2, I_t = \frac{4n_1 n_2}{(n_1 + n_2)^2} \tag{2}$$

with $n_1 = 1.00$ the refractive index of air and n_2 the refractive index of the alginate solution (close to water, Section 3.2) or of dry alginate (Section 3.4).[47] Multiple reflection paths from the film interfere with each other. The reflection from the front side of the film carries the relative intensity I_r and undergoes a phase shift of π. Light that passes the film thickness h for $2N$ times undergoes a phase shift of $2\pi 2Nn_2 h\lambda^{-1}$ and carries the relative intensity $I_r^{(2N-1)}\ I_t^2$ with λ the wavelength. Superposing all reflected contributions yields the spectrum of reflected light. To compute the visual color impression in Figures 5III and 7II, the reflected spectrum is multiplied with the CIE 1964 color matching functions. The result was transferred to RGB for plotting by

$$\mathrm{RGB} = \mathbf{M} \cdot XYZ \tag{3}$$

with

$$M = \begin{matrix} 3.1338561 & -1.6168667 & -0.4906146 \\ -0.9787684 & 1.9161415 & 0.0334540 \\ 0.0719453 & -0.2289914 & 1.4052427 \end{matrix} \tag{4}$$

3. Results

The present study focuses on an alginate-based system, the chemistry of the system remaining identical throughout the paper at hand. We first discuss the interfacial and bulk properties of the system in its liquid state (Section 3.1) to choose an appropriate formulation and to provide a frame of reference for the drainage behavior of the liquid films. We use surface tensiometry results (Section 3.1.1) to determine whether the alginate adsorbs at the air-liquid interface. In Section 3.1.2, we show the viscosity of alginate solutions at various concentrations and determine the concentration range of the solution used for thin-film experiments. We then show film drainage for the non-gelling solution to provide a reference behavior for drainage at two capillary pressures, namely 500 and 2000 Pa (Section 3.2). We continue with an investigation of the kinetics of gelation of the system via oscillatory rheology (Section 3.3) to precisely match the advancement of gelation and film drainage in the μTFPB. Finally, we present in Section 3.4 the drying experiments within the μTFPB with the various film morphologies obtained for the different experimental conditions.

3.1. Characterization of the Non-gelling Solution

3.1.1. Surface Tension

To gain insight into the interfacial properties of the investigated solution, we characterized the surface tension of a 1 wt% alginate solution, in the presence and in absence of the Ca/EGTA and the surfactant. The results are shown in **Figure 3**. The pure alginate solution shows a slow relaxation, approaching an equilibrium surface tension of $(57.7 \pm 1.0) \times 10^{-3}$ N m^{-1}. This surface tension decrease seems to indicate that alginate is surface active at long timescales. This has been reported in the literature and may be associated with the slightly hydrophobic nature of the protonated carboxyl groups protruding above the air–water interface while the hydrophilic, deprotonated carboxyl groups remain in the water.[48–51] When using the 1 wt% alginate solution with 0.001 M Ca/EGTA, the overall relaxation remains very similar with a slight increase of the equilibrium surface tension to $(60.6 \pm 1.0) \times 10^{-3}$ N m^{-1}.

Upon addition of 0.5 wt% surfactant Glucopon 600 CSUP to alginate and Ca/EGTA, the surface tension relaxes very rapidly

© 2022 The Authors. Macromolecular Rapid Communications published by Wiley-VCH GmbH

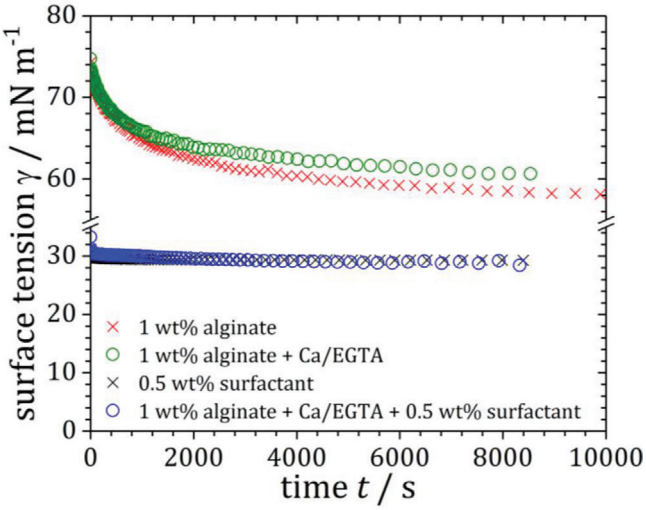

Figure 3. Surface tension of solutions of increasing complexity leading to the complete formulation used for the gelling experiments. The Ca/EGTA concentration is 0.001 M and the surfactant is Glucopon 600 CSUP.

(within 10 s) to its equilibrium value of $(29.1 \pm 0.2) \times 10^{-3}$ N m^{-1}. This value is very close to the surface tension of pure Glucopon 600 CSUP solutions of $(29.3 \pm 0.2) \times 10^{-3}$ N m^{-1}. We can thus assume that the surface of the solution used for the thin film studies is fully covered with the Glucopon surfactant and that the effects that alginate and Ca/EGTA have on the surface tension are negligible in the presence of a high concentration of surfactant. Since Glucopon is a nonionic alkyl polyglycoside we do not expect any aggregation between the surfactant and the negatively charged polymer. Although some weak hydrogen interactions may act between the surfactant and the alginate, these would not be strong enough to alter the conformation of the alginate chains in solution.[52] The lack of affinity of the alginate for the interface in presence of surfactant is a valuable advantage for the gelling film experiments (see Section 3.4), as one can therefore assume that the interface does not gel along with the "bulk" of the film, meaning that the viscoelastic properties of the interface should remain unchanged throughout gelation.

3.1.2. Viscosity of Alginate Solutions

Figure 4a shows how the viscosity varies with shear rate for the example of a 1 wt% alginate solution containing i) no additives, ii) 0.001 M Ca/EGTA, and iii) 0.001 M Ca/EGTA with 0.5 wt% Glucopon 600 CSUP (the surfactant). The last solution corresponds to the solution used in Sections 3.2 and 3.3 (without GDL, which triggers cross-linking). We see that all solutions follow a shear-thinning behavior obeying the Cross model (dashed lines, all fitting parameters are provided in Table S1, Supporting Information). First, one notices that the zero-shear viscosity depends on the presence of surfactant and/or Ca/EGTA. The pure alginate solution has the highest zero-shear viscosity, while the alginate with Ca/EGTA and surfactant is the least viscous. One may attribute this difference in viscosities to the screening of the negative charges of alginate as the ionic strength of the solution increases: i) The pure alginate solution does not contain any added ions (i.e., no other ions than the sodium ions brought by the alginate itself). ii) Since after addition of Ca/EGTA the solution is brought back to a neutral pH by addition of NaOH (see Section 2.2.1), the ionic strength of solutions containing Ca/EGTA is increased. iii) Upon further addition of surfactant, the viscosity decreases further, which may come from ionic impurities. Although Glucopon 600 CSUP is an alkyl polyglycoside and is therefore non-ionic, it is a technical surfactant and negatively charged impurities originating from its synthesis may remain.[53] There may also be some weak interactions between the surfactant and the polymer, as discussed in Section 3.1.1.

We use the fits to the Cross model to determine the zero-shear viscosity of pure alginate solutions at different alginate concentrations (blue curve in Figure 4b). As expected, the viscosity increases rapidly with increasing alginate concentration. One can distinguish two regimes with two different slopes. Below an alginate concentration of ca. 0.25 wt%, the viscosity follows a power law of exponent ≈ 0.7 with the concentration, which is between 0.6 and 1.3 and thus corresponds to the semidilute unentangled regime.[54,55] Above a concentration of 0.25 wt% alginate, the viscosity follows a power law of exponent ≈ 2.6. Such a strong dependency of the viscosity on the concentration is typical in polyelectrolyte solutions in the semi-dilute entangled regime.[54,55] In the latter regime, we also measured the viscosity of the complete solutions containing Ca/EGTA and the surfactant (red curve in Figure 4b). Although the viscosities systematically lie below those of the pure alginate solutions, which is in line with the observations from Figure 4a, the viscosity follows globally the same power law. One can thus conclude that the addition of Ca/EGTA and surfactant to the alginate slightly lowers the viscosity of the solution (probably through the screening of charges) but does not intrinsically alter the behavior of the alginate chains in solution.

To ensure homogeneous gelation of the solutions, it is advisable to work in the semi-dilute entangled regime. Therefore, we chose in the following to conduct all further experiments at a concentration of 1 wt% alginate + 0.001 M Ca/EGTA + 0.5 wt% surfactant (arrow in Figure 4b). This solution has a zero-shear viscosity of (0.47 ± 0.20) Pa s.

3.2. Drainage of Non-gelling Films

First, we carried out film drainage experiments in the μTFPB with non-gelling films at two different capillary pressures p_c using the formulation identified in Section 3.1.2. **Figure 5**I,II shows examples of characteristic image sequences of films submitted to p_c = 500 Pa (Figure 5I) and p_c = 2000 Pa (Figure 5II). The images were chosen at moments which represent a similar stage of evolution in the film thickness profile. They correspond to different times for the different pressures, as discussed later. Globally, at both capillary pressures, the films show a similar drainage behavior, starting from a thick lens-like film forming a thicker zone (the "dimple"[56,57]) in its center (Figure 5I,IIa). This dimple expands together with the film. The bright colors indicate film thicknesses in the range of 100–1000 nm[56,57] (Figure 5I–IIb,III). The films drain further until black regions appear (Figure 5I–IIc), commonly called Newton black films (NBFs), which correspond to a hydrated surfactant bilayer of ca. 5–15 nm in thickness.[35,31] One may thus assume that the black regions are depleted of

© 2022 The Authors. Macromolecular Rapid Communications published by Wiley-VCH GmbH

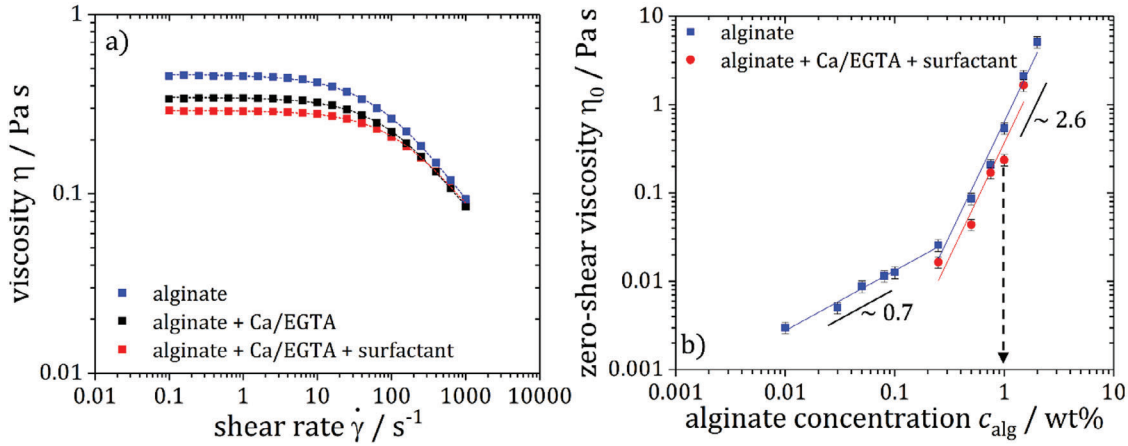

Figure 4. a) Viscosity of 1 wt% alginate solutions without additives, with 0.001 M Ca/EGTA and 0.001 M CA/EGTA + 0.5 wt% surfactant (Glucopon 600 CSUP). The dotted lines correspond to the fit by the Cross model for each solution (the Cross model parameters are reported in Table S1 of the Supporting Information). b) Viscosity of alginate solutions as a function of the alginate concentration without additives and 0.001 M Ca/EGTA + 0.5 wt% surfactant (Glucopon 600 CSUP). The lines are best fits to a power law. The error bars correspond to the largest error of the average over three measurements for each of the solutions from a), which was reported to all the data points. The dotted arrow shows the alginate concentration used in this article for the thin film investigations.

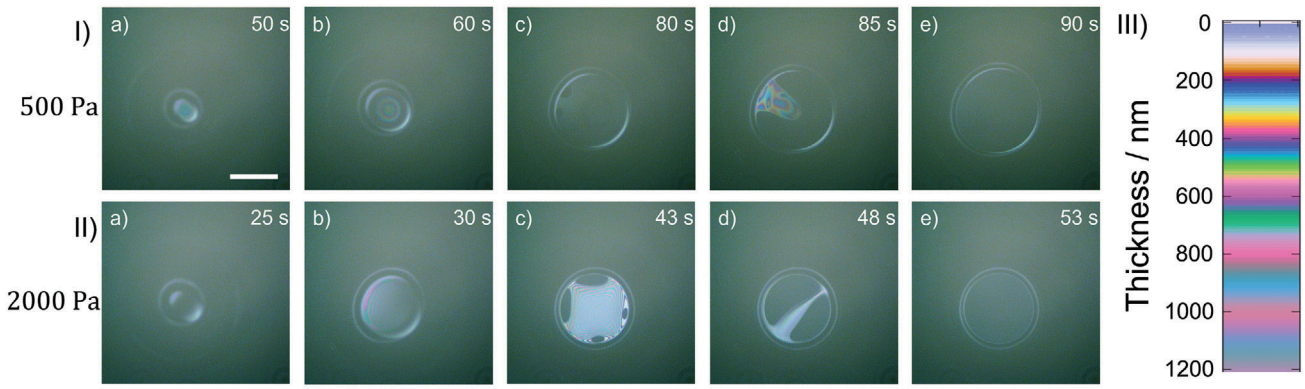

Figure 5. Drainage of non-gelling alginate films at different capillary pressures: I) p_c = 500 Pa and II) p_c = 2000 Pa. All images are at the same scale and the scale bar is 250 µm. $t = 0$ is taken when the capillary pressure p_c is applied. III) Colorimetric map of the film thickness calculated for water.

polymer.[58,59] The NBF region(s) keep expanding (Figure 5I–IIc) until a full Newton black film is reached (Figure 5I–IIe). We do not see "Common Black Films"[31] since the surfactant is non-ionic and the natural surface charges of the gas/water interface are screened by the ionic nature of the alginate and the additives. Although showing similar drainage characteristics, a higher capillary pressure induces faster film drainage. When draining at p_c = 500 Pa, the first NBF appears after 80 s, while the first NBF appears after 40 s at p_c = 2000 Pa. Similarly, the film has reached its full NBF state after 90 s at p_c = 500 Pa whereas it took 53 s for the film at p_c = 2000 Pa to reach equilibrium.

As a first order approximation, the characteristic drainage time τ_d of the film may be approximated as[60,61]

$$\tau_d \sim \frac{\eta}{p_c}\left(\frac{R}{h}\right)^{\beta} \tag{5}$$

with η being the viscosity of the fluid, p_c the capillary pressure, R the film radius, h the film thickness. β is a dimensionless exponent set by the boundary conditions, i.e., by the viscoelastic properties (interfacial rheology) of the interfaces. For a free-slip boundary condition (fully "mobile" interfaces leading to a plug flow), $\beta = 0$, while for the no-slip condition ("immobile" or "rigid" interfaces leading to a Poiseuille flow),[60,61] $\beta = 2$. Most systems lie between these two idealized cases.[57,60,61] We chose here to keep a constant surfactant concentration to avoid adding the interfacial rheology of the system as a tuning parameter. As interfacial rheology can be a crucial parameter in the drainage behavior of thin liquid films,[37,62,63] its effect on the drainage and rupture of gelling films deserves its own study and is left out of the paper at hand.

We see from Equation (5) that the characteristic drainage time varies inversely with the capillary pressure, which is verified to first approximation by our observations from Figure 5, where the drainage is approximately two times faster for p_c = 2000 Pa than for p_c = 500 Pa. Moreover, one can observe a rapid jump in film thickness from thick regions (colorful regions with thicknesses above several hundreds of nm) directly to a NBF (Figure 5I–IIc,d).

© 2022 The Authors. Macromolecular Rapid Communications published by Wiley-VCH GmbH

Table 1. Rheological properties of the gelling bulk alginate solutions corresponding to the three film experiments (A,B,C).

Experiment	p_c [Pa]	t_{gel} [min]	t/t_{gel} at drainage	t/t_{gel} at drying	G' at drainage [Pa]	G'' at drainage [Pa]	G' at drying [Pa]	G'' at drying [Pa]
A	2000	259	0.40	0.47	0.48	2.48	0.56	2.60
B	2000	310	0.54	0.57	0.77	3.00	0.88	3.09
C	500	289	0.41	0.56	0.44	2.33	0.67	2.71

This suggests the presence of strong attractive forces, likely due to depletion forces arising from the polyelectrolytes (or, more precisely, their counter-ions).[54] A similar drainage behavior was observed in thin liquid films containing wormlike micelles.[64] Further experiments are underway to quantify this effect and to validate this hypothesis.

No film broke within the experimental time (≈ 5 min), indicating that even though the Newton Black Films are very thin, they are very stable within the μTFPB. Alkyl polyglycosides are known to make stable Newton Black Films for capillary pressures up to several kPa.[65,66] Moreover, the μTFPB device is designed to dampen vibrations and the atmosphere surrounding the film is saturated with water to prevent evaporation in order to improve film stability.[35]

3.3. Rheological Characterization of the Gelling Systems

We induced gelation via the addition of 1.25 wt% GDL into the 1 wt% alginate solution containing calcium ions chelated with EGTA (0.001 M Ca/EGTA) following the protocol described in Section 2.2.1. GDL self-hydrolyses over time, inducing an acidification which results in the release of the calcium ions from the EGTA and the physical cross-linking of the alginate by the calcium ions.[67]

We carried out oscillatory rheology at $f = 1$ Hz (Section 2.2.3) to follow the kinetics of gelation in parallel with the thin film experiments described in Section 3.4. **Figure 6** shows the evolution of the storage modulus G' and loss modulus G'' with the relative time t/t_{gel}, t_{gel} being the gel point given in **Table 1**. Both moduli increase with time in a well-known manner for gel formation, showing a cross-over that we took as the gel point. We show results for three experiments A, B, and C, for which we present film studies in Section 3.4. The relative kinetics of gelation collapse well for all experiments with $G' = G'' \approx 5.4$ Pa at the gel point. However, the gel time varies between 259 min and 310 min for the different experiments. We attribute the differences in the gel times to uncertainties in weighing the GDL and differences in the lab temperature before the samples were put in the temperature-controlled rheometer (20 min elapsed between the addition of GDL into the alginate solution to the start of the oscillatory rheology measurement). Note that the gel times are always two orders of magnitude larger than the film drainage times as determined in Section 3.2, allowing us to start film drainage over a long timeframe before gelation. Long gel times also allow us to set the μTFPB experiment up and form the lens-like film before the alginate solution becomes too viscoelastic (see Section 2.2.4), making the experiments with gelling films as close as possible to the ones with non-gelling films.

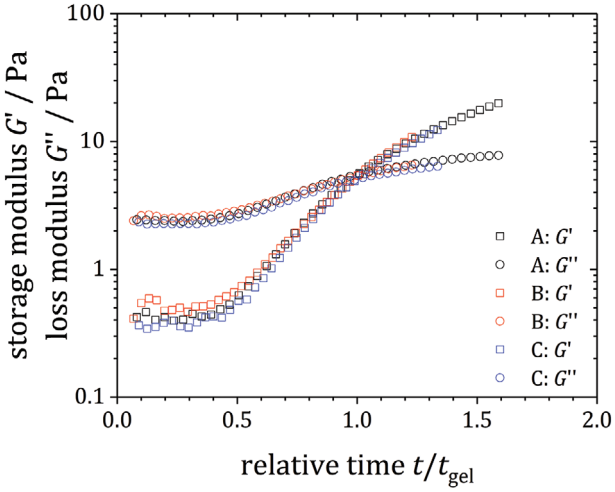

Figure 6. Gelation kinetics of the alginate-based system (1 wt% alginate, 0.001 M Ca/EGTA, 0.5 wt% Glucopon 600 CSUP) for the experiments A, B, and C, at a frequency of $f = 1$ Hz and a strain of 1%. Gelation was triggered by acidification via addition of 1.25 wt% GDL at $t = 0$ s. The time t has been normalized by the gel time t_{gel}, taken at the crossover between G' and G''. The gel times are: A: 259 min; B: 310 min; C: 289 min (see Table 1).

To have the best precision possible on the rheological properties of the gelling alginate film as the film drains in the μTFPB, we carried out the oscillatory rheology measurements in parallel with the μTFPB experiments shown in Section 3.4, i.e., we used part of the solution after addition and dissolution of GDL for characterizing the kinetics of gelation and the rest of the same solution for the generation of gelling films in the μTFPB. The experiments A, B, and C in Figure 6 correspond to the films A, B, and C in **Figure 7** and in Table 1.[68,16]

3.4. Drying of Films undergoing Gelation

Goal of these experiments is to mimic as closely as possible the behavior of a liquid foam undergoing 1) bubble compaction through the capillary pressure, 2) gelation and 3) drying at the scale of an isolated free-standing film. To this end, we wait for the initial liquid lens in the μTFPB to cross-link for a given time t/t_{gel} (well before the gel point) and subsequently apply a given capillary pressure p_c (500 or 2000 Pa) to drain the film. The latter corresponds to the foaming step in the generation of a hydrogel foam from a liquid foam template, as the capillary pressure in a foam originates from its structure (Equation 1, Section 1).[24,25] Once the film stops evolving under the applied capillary pressure (typically after 15 min), we allow a slow gas flow around the film to initiate the drying process (Section 2.2.4).

© 2022 The Authors. Macromolecular Rapid Communications published by Wiley-VCH GmbH

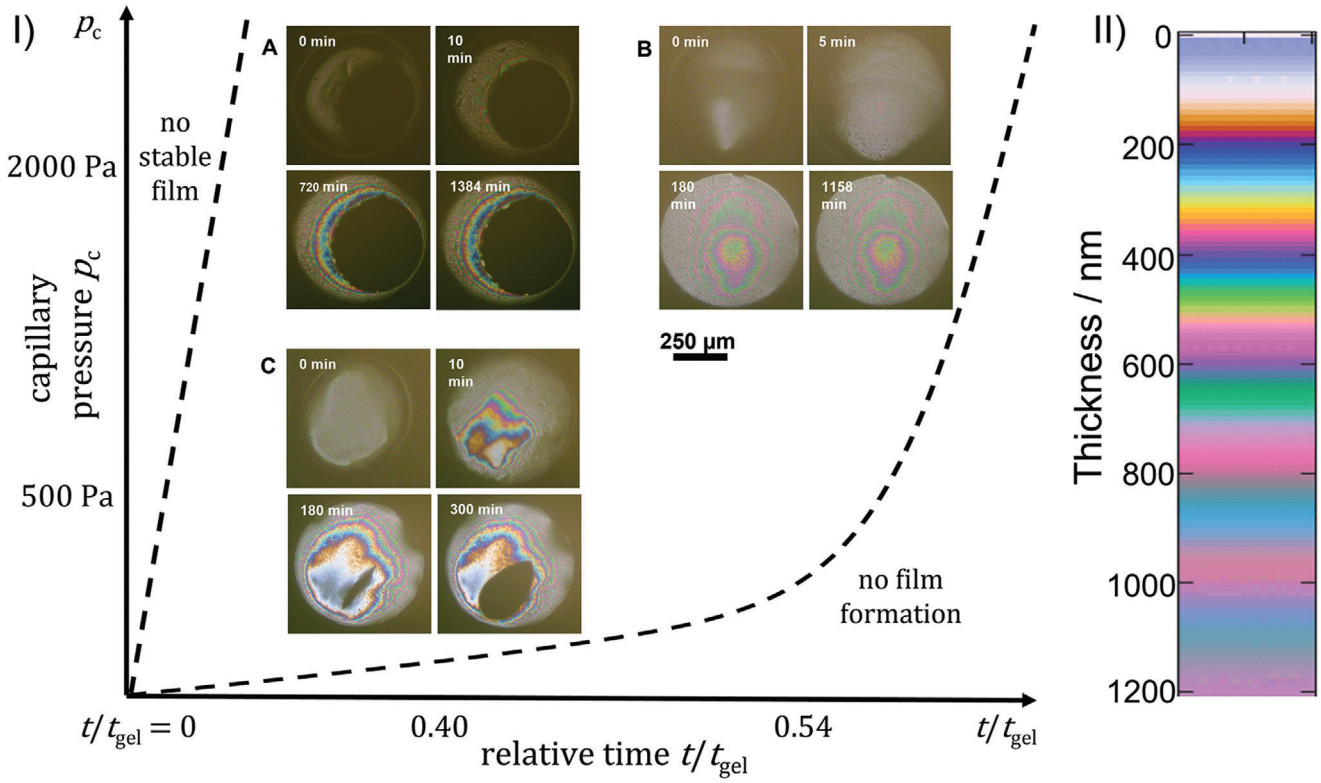

Figure 7. I) Diagram showing the drying of thin films undergoing gelation which were drained at different capillary pressures and relative times, i.e., $t/t_{gel} \approx 0.4$ and 0.54. $t = 0$ min in the photographs corresponds to the start of drying, which was initiated after drainage stopped. All images are at the same scale. The films A, B and C correspond to the experiments in Figure 6 and Table 1. II) Colorimetric map of the film thickness calculated for dry alginate.

We show here the results of three characteristic experiments, A, B, and C. Their kinetics of gelation are shown in Figure 6, while Table 1 gathers their viscoelastic properties at the times of interest (drainage and drying).

Figure 7I shows how the different films evolve from the drained stage until being fully dried depending on the capillary pressure p_c and the relative time t/t_{gel} upon draining, related to the cross-linking degree. At sufficiently high capillary pressures and far from the gel point, the film breaks immediately as drying starts (zone "no stable film" in Figure 7I). Too close to the gel point, the thick lens cannot be deformed into a film since the solution is too viscoelastic (zone "no film formation" in Figure 7I). This is probably due to a finite yield stress after a given cross-linking degree which cannot be overcome by the applied capillary pressure. Therefore, the solution cannot be pressed out of the liquid lens and no film is formed. In-between these extreme zones, films can be formed, drained, and dried, showing very different behavior depending on their position in the (p_c, t/t_{gel}) diagram (Figure 7I).

Figure 7IA–C shows image sequences obtained during the drying process of three different films that were drained at different (p_c, t/t_{gel}) couples. Note that the gelling solution contains 1 wt% of alginate and 0.5 wt% surfactants. The films therefore lose almost 98.5 wt% of their mass upon drying. As summarized in Table 1, film A was drained at $p_c = 2000$ Pa and at a relative time $t/t_{gel} = 0.40$. Film B was also drained at $p_c = 2000$ Pa but at a later relative time $t/t_{gel} = 0.54$. Finally, film C was drained at $p_c = 500$ Pa but at a relative time close to that of film A, i.e., $t/t_{gel} = 0.41$.

Looking at film A in Figure 7I, even before drying, the gelling film formed a circular Newton Black Film (NBF) surrounded by a thick heterogeneous bulge ($t = 0$ min). The NBF looks like a black hole, but it is actually composed of a hydrated surfactant layer, as discussed in Section 3.2. The NBF expands during drying and the rim becomes increasingly colorful ($t = 10$ and 720 min). This is because the drying leads to an increasingly thin film, strengthening the contrast between different colors in the reflected light. We cannot measure reliably the film thickness, since we do not know precisely the refractive index of the dried film, but we can estimate it to be of the order of 100–400 nm using the literature value of the refractive index of pure alginate (approximately 1.38)[47] to produce a color map (Figure 7II).

Comparing the film after 720 and 1384 min, one sees that the film stopped evolving after 720 min meaning that it is completely dried. Note that the NBF broke to form a hole during drying, but NBFs are so thin and reflect so little light that the exact point at which the NBF broke remains unknown. The final film therefore contains a large hole of the same shape as the circular NBF it originated from, although larger. Such a circular opening has been previously observed in the literature (see Figure 1b-B) and such a morphology was coined as "pinhole,"[69] sometimes surrounded by a bulge (see Figure 1b-C).

The gelling film in Figure 7IB is very thick when the drying process is started ($t = 0$ min) and does not show any NBF region.

© 2022 The Authors. Macromolecular Rapid Communications published by Wiley-VCH GmbH

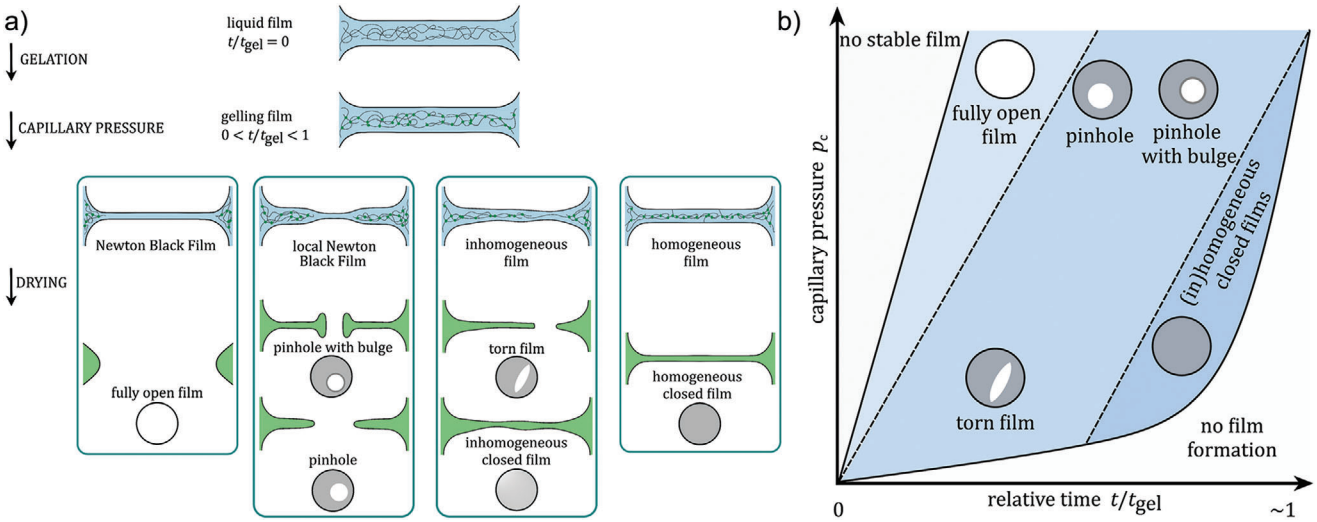

Figure 8. a) Phenomenological description of the expected structures of dried hydrogel films from drying various morphologies of drained hydrogel films. The surfactants are not represented on the figure for the sake of clarity. b) Diagram showing the possible film morphologies following the drainage and drying of gelling films, as a function of the two parameters p_c and t/t_{gel}.

Upon drying, the film thins, which is visible by the colors. We can estimate the film thickness to be larger than a few hundred nanometers. The film remains fully intact with a central zone which is about 500 nm thinner than the film border (Figure 7II) but remains itself thicker than 500 nm. The film stops evolving after 180 min, indicating that it is completely dried. One can thus assume that a foam generated in the same condition of capillary pressure and at the same cross-linking stage would remain closed-cell as the example in Figure 1b-A.

Finally, the film formed at lower p_c and t/t_{gel} is also initially very thick (Figure 7IC) and heterogeneous, and does not present any NBF region. Similar to the film B, it thins upon drying, creating a thinner zone in the central lower part of the film which becomes first white and then gray, indicating a film thickness of less than 100 nm (Figure 7II), while the rim of the film remains a few hundred nm thick. After 180 min, this thinner region ruptures and a tear appears while other regions of the film continue thinning. Upon further drying, the tear continues expanding, reaching a slightly elliptic shape. Such film opening process would lead to open-cell foams. Open-cell foams with irregularly shaped holes seemingly originating from a tear have also been reported in the literature, as seen in Figure 1b-E.

We can see from this set of experiments that by using the same formulation but different processing conditions, very different dry film morphologies can be obtained. In very general terms one can say that the capillary pressure p_c and the relative time at which the capillary pressure is applied (t/t_{gel}) control the thickness profile of the film obtained at the end of drainage. The thickness profile of the drained film controls the fate of the film during the drying process together with the viscoelastic state of the film. Within the (p_c, t/t_{gel})-ranges where films can be obtained, one can already distinguish two important categories. The first category arises when capillary pressures are sufficiently high and the film sufficiently fluid during drainage (small t/t_{gel}) so that one (or more) polymer-free zones (NBF) are formed in the film before drying. These zones will naturally rupture during drying. Since the shape of these zones is imposed when the film is still fluid, they are fairly circular in shape, leading to neat pinhole-type pore connections. The second category is the one in which the entire film contains polymer before drying. This scenario is obtained when the capillary pressure is sufficiently low and/or the crosslinking advanced enough to avoid strong film drainage. When the drained film is sufficiently thick and homogeneous, it merely thins during the drying process maintaining its integrity. However, if the film locally contains much thinner zones, the stresses created through shrinkage upon drying and crosslinking are localized in the thin zones and may lead to a tear in the film. Since the film is already solid-like at this stage, the tear expands during further drying but maintains its characteristic "tear-shaped" form.

4. Discussion

We have seen in Section 3.4 that different couples of capillary pressure p_c and relative time t/t_{gel} yield dried films of very different morphologies. One can see in Figure 7I that both p_c and t/t_{gel} have an influence on the morphology of the drained film, which in turn affects the morphology of the dried film. Combining our different observations and conclusions from Section 3.4 with what is known from the literature, we propose in **Figure 8**a a phenomenological diagram showing how different morphologies of drained films may yield a given morphology of dried films.

The proposed scenarios are limited by two extreme cases: 1) When p_c is too high and t/t_{gel} too low, films break already in the liquid state ("no stable film", Figure 8b). In the initially liquid foam, this leads to foam collapse. 2) When p_c is too low and t/t_{gel} too high, the thick lens cannot be deformed into a thin film due to the finite yield stress of the viscoelastic liquid ("no film formation", Figure 8b). It will be important in future work to quantify this yield stress and to relate it to the characteristic stresses arising in the liquid lens to define this limit more quantitatively.

© 2022 The Authors. Macromolecular Rapid Communications published by Wiley-VCH GmbH

In between these two limits, different scenarios may arise depending on the position of the system in the (p_c, t/t_{gel}) diagram (Figure 8b). At sufficiently high p_c and low t/t_{gel}, a Newton Black Film (NBF) is formed in the drained film. Since the NBF does not contain polymer, it yields a hole in the dried state (for example film A in Figure 7I). If the NBF spans across the entire film, the final film would be "fully open," leading to a fully open-cell foam. If the NBF covers only part of the film, its rupture during drying would lead to a "pinhole." This pinhole generally expands upon drying and may also form a bulge depending on the capacity of the viscoelastic matrix to flow.[70] Future studies need to establish more quantitative relationships between the hole shape and the film viscoelasticity.

At lower p_c and higher t/t_{gel}, the drained film may contain polymer everywhere. The drained film can then be homogeneous or inhomogeneous in thickness. In both cases, film rupture before drying is unlikely. The simplest case is that both films dry without rupture, leading to (in)homogeneous dry films which are fully closed. Film B in Figure 7I is an illustrative example of this scenario. These films, in turn, lead to fully closed foams. However, as shown in the film C of Figure 7I, the contraction of the films during drying and further cross-linking may lead to sufficiently high stresses within the film to lead to a fracture. This is most likely to occur in the thinnest part of inhomogeneous films where stresses are concentrated and where the film is most fragile. This fracture is likely to expand during the drying process, due to the increasing film stresses. However, in contrast to the pinhole, its shape will remain irregular, due to the solid-like nature of the surrounding film. Independently of the precise hole shape, this fracture will lead to open-cell foams.

Although we see in Figure 8b that the consideration of the capillary pressure p_c and relative time t/t_{gel} upon draining allows to establish different categories of film fates, the use of t/t_{gel} clearly oversimplifies the consideration of the viscoelastic properties of the bulk phase upon cross-linking. Future work needs to be based on a more complete investigation of the evolution of the viscoelastic properties during gelation (viscosity, yield stress, shear modulus) and how they influence the different drainage and drying stages. Moreover, one also needs to consider that different effects (depletion, confinement effects, etc.) are likely to lead to non-negligible inhomogeneities in the film whose local evolution may differ significantly from the bulk gel.[68] Indeed, the micro- to nanometric dimensions of the films within the μTFPB may induce changes of the polymer conformations which, in turn, may affect the kinetics of gelation. Although this effect has been investigated in hydrogels from low-molecular-weight gelators,[16] such an experimental investigation is still lacking for polymeric hydrogels. Resolving this crucial question is out of the scope of the paper at hand, and we therefore assumed here that any effect of soft confinement on the kinetics of gelation is either negligible or constant throughout all samples. Future work will have to address this question to provide an accurate characterization of the evolution of the viscoelastic properties of the film upon drainage and drying. Further developments of the μTFPB and its coupling with other characterization methods such as X-ray or neutron scattering are necessary to provide a more quantitative understanding of the competition between the capillary pressure and the viscoelastic properties of the gelling film.

5. Conclusion and Outlook

We used a home-built microfluidic thin-film pressure balance (μTFPB) to show its potential for the investigation of pore-opening processes in hydrogel foams at the scale of isolated free-standing films. We focused on a single alginate-based gelling system and varied the relative timescales of drainage and gelation by varying the capillary pressure p_c and the relative time t/t_{gel}. We demonstrated that within this simple framework one already has access to a wide range of film morphologies upon draining and drying. We showed for the first time isolated films forming a hole/crack while not leading to complete film rupture within a thin film pressure balance. We provided a first phenomenological description of the different pore-opening mechanisms at play in these films, and we claim that they can be related to pore-opening mechanisms in hydrogel foams. We also showed that a single formulation can lead to at least three different thin film morphologies, simply by tuning physical parameters such as the capillary pressure and the relative time t/t_{gel}. While previous research mainly focused on modifications of the chemistry/physical chemistry of the system (e.g., the concentration of the polymer/surfactant),[3,9,27] our experiments confirm that physical parameters linked to the foaming process and foam morphology are also important levers to fine-tune foam connectivity.[22,23]

We provide here a very simple framework to explain characteristic film morphologies which depend on the capillary pressure and the relative time t/t_{gel}. Future work needs to refine this framework, e.g., by identifying the decisive viscoelastic properties (both of the bulk and the interface). In this process, questions of gelation in the vicinity of interfaces and under (soft) confinement need to be addressed and their influence on pore-opening processes needs to be established. For this purpose, it will be essential to improve the μTFPB by coupling it with more elaborate techniques to measure the drainage and rupture of the solidifying film more quantitatively. Moreover, the drying protocol needs be optimized to be closer to the drying process(es) arising in foams. In many practical cases, hydrogel foams are actually freeze-dried. Further studies will therefore have to consider different drying protocols and their influence on the final film morphology. For example, freeze-drying may lead to morphologies such as the partially open film seen in Figure 1b-D.

To reduce some of the complexity, we worked here with systems in which the gel time is larger than the characteristic experimental time. Since many systems used for foaming gel more rapidly, future work also needs to address how the gelation kinetics influences film drainage and rupture.

We also worked with one surfactant type only that makes highly stable films with mobile interfaces that are not involved in the cross-linking process of the bulk film. Future investigations need to vary systematically the surfactant type to investigate its manifold influences on the drainage and cross-linking process of the bulk film.

Last but not least, even though we chose a hydrogel as a model system, we are confident that the methods introduced in this paper apply to non-aqueous polymer foams such as, e.g., polyurethane foams.

© 2022 The Authors. Macromolecular Rapid Communications published by Wiley-VCH GmbH

Supporting Information

Supporting Information is available from the Wiley Online Library or from the author.

Acknowledgements

The authors acknowledge funding from an ERC Consolidator Grant (agreement 819511 - METAFOAM), from the region Grand Est (Young Investigator Grant), and from the Interdisciplinary Institute "Hierarchical Functional Materials" supported by IdEx Unistra (ANR-1″0-IDEX-0002) and SFRI (STRAT'US project, ANR-20-SFRI-0012) under the framework of the French Investments for the Future Program.

Conflict of Interest

The authors declare no conflict of interest.

Data Availability Statement

The data that support the findings of this study are available on request from the corresponding author. The data are not publicly available due to privacy or ethical restrictions.

Keywords

alginate, film rupture, free-standing thin films, hydrogel foams, pore-opening

Received: February 26, 2022
Revised: April 21, 2022
Published online:

[1] D. Eaves, *Handbook of Polymer Foams*, Rapra Technology Limited, Shawbury **2004**.
[2] N. Mills, *Polymer Foams Handbook: Engineering and Biomechanics Applications and Design Guide*, Elsevier Science & Technology, Oxford **2007**.
[3] A. Quell, B. De Bergolis, W. Drenckhan, C. Stubenrauch, *Macromolecules* **2016**, *49*, 5059.
[4] X. Liu, P. X. Ma, *Biomaterials* **2009**, *30*, 4094.
[5] A. Salerno, S. Iannace, P. A. Netti, *Macromol. Biosci.* **2008**, *8*, 655.
[6] F. Dehghani, N. Annabi, *Curr. Opin. Biotechnol.* **2011**, *22*, 661.
[7] M. Costantini, C. Colosi, P. Mozetic, J. Jaroszewicz, A. Tosato, A. Rainer, M. Trombetta, W. Święszkowski, M. Dentini, A. Barbetta, *Mater. Sci. Eng. C* **2016**, *62*, 668.
[8] C. Gaulon, J. Pierre, C. Derec, L. Jaouen, F. - X. Bécot, F. Chevillotte, F. Elias, W. Drenckhan, V. Leroy, *Appl. Phys. Lett.* **2018**, *112*, 261904.
[9] V. H. Trinh, V. Langlois, J. Guilleminot, C. Perrot, Y. Khidas, O. Pitois, *Mater. Des.* **2019**, *162*, 345.
[10] P. X. Ma, J.-W. Choi, *Tissue Eng.* **2001**, *7*, 23.
[11] J. M. Karp, P. D. Dalton, M. S. Shoichet, *MRS Bull.* **2003**, *28*, 301.
[12] R. Deleurence, T. Saison, F. Lequeux, C. Monteux, *Soft Matter* **2015**, *11*, 7032.
[13] I. Maimouni, M. Morvaridi, M. Russo, G. Lui, K. Morozov, J. Cossy, M. Florescu, M. Labousse, P. Tabeling, *ACS Appl. Mater. Interfaces* **2020**, *12*, 32061.
[14] A. K. Singh, A. Shishkin, T. Koppel, N. Gupta, *Composites, Part B* **2018**, *149*, 188.
[15] G. Wypych, *Handbook of Foaming and Blowing Agents*, ChemTec Publishing, Toronto **2017**.
[16] Y. Liu, W.-J. Zhao, J.-L. Li, R.-Y. Wang, *Phys. Chem. Chem. Phys.* **2015**, *17*, 8258.
[17] L. Braun, M. Kühnhammer, R. Von Klitzing, *Curr. Opin. Colloid Interface Sci.* **2020**, *50*, 101379.
[18] E. Chatzigiannakis, J. Vermant, *Soft Matter* **2021**, *17*, 4790.
[19] E. Chatzigiannakis, J. Vermant, *Phys. Rev. Lett.* **2020**, *125*, 158001.
[20] E. S. Minina, P. A. Sánchez, C. N. Likos, S. S. Kantorovich, *J. Mol. Liq.* **2019**, *289*, 111066.
[21] D. Langevin, *Phys. J.* **2004**, *3*, 67.
[22] A. Testouri, M. Ranft, C. Honorez, N. Kaabeche, J. Ferbitz, D. Freidank, W. Drenckhan, *Adv. Eng. Mater.* **2013**, *15*, 1086.
[23] F. Dehli, A. Southan, W. Drenckhan, C. Stubenrauch, *J. Colloid Interface Sci.* **2020**, *588*, 326.
[24] I. B. Djemaa, S. Auguste, W. Drenckhan-Andreatta, S. Andrieux, *Adv. Colloid Interface Sci.* **2021**, *294*, 102478.
[25] S. Andrieux, A. Quell, C. Stubenrauch, W. Drenckhan, *Adv. Colloid Interface Sci.* **2018**, *256*, 276.
[26] C. Stubenrauch, A. Menner, A. Bismarck, W. Drenckhan, *Angew. Chem., Int. Ed.* **2018**, *57*, 10024.
[27] M. Costantini, C. Colosi, J. Guzowski, A. Barbetta, J. Jaroszewicz, W. Święszkowski, M. Dentini, P. Garstecki, *J. Mater. Chem. B* **2014**, *2*, 2290.
[28] M. S. Silverstein, *Prog. Polym. Sci.* **2014**, *39*, 199.
[29] S. Andrieux, L. Medina, M. Herbst, L. A. Berglund, C. Stubenrauch, *Composites, Part A* **2019**, *125*, 105516.
[30] L. J. Gibson, M. F. Ashby, *Cellular Solids: Structure and Properties*, Cambridge University Press, Cambridge **1999**.
[31] L. Gong, S. Kyriakides, W.-Y. Jang, *Int. J. Solids Struct.* **2005**, *42*, 1355.
[32] J. G. Lundin, G. C. Daniels, C. L. Mcgann, J. Stanbro, C. Watters, M. Stockelman, J. H. Wynne, *Macromol. Mater. Eng.* **2017**, *302*, 1600375.
[33] S. Andrieux, *Monodisperse Highly Ordered and Polydisperse Biobased Solid Foams*, Springer International Publishing, Cham, Switzerland **2018**.
[34] C. Poulard, S. Levannier, A. Gryson, M. Ranft, W. Drenckhan, *Adv. Eng. Mater.* **2017**, *19*, 1600534.
[35] S. Andrieux, P. Muller, M. Kaushal, N. S. Macias Vera, R. Bollache, C. Honorez, A. Cagna, W. Drenckhan, *Lab Chip* **2021**, *21*, 412.
[36] W. Drenckhan, A. Saint-Jalmes, *Adv. Colloid Interface Sci.* **2015**, *222*, 228.
[37] C. Stubenrauch, R. V. Klitzing, *J. Phys.: Condens. Matter* **2003**, *15*, R1197.
[38] E. Chatzigiannakis, P. Veenstra, D. Ten Bosch, J. Vermant, *Soft Matter* **2020**, *16*, 9410.
[39] D. L. Weaire, S. Hutzler, *The Physics of Foams*, Clarendon Press, Oxford **1999**.
[40] I. Cantat, S. Cohen-Addad, F. Elias, F. F. F. Graner, R. Höhler, O. Pitois, F. Rouyer, A. Saint-Jalmes, in *Foams – Structure and Dynamics* (Ed: S. J. Cox Oxford University Press, Oxford **2013**.
[41] W. Drenckhan, S. Hutzler, *Adv. Colloid Interface Sci.* **2015**, *224*, 1.
[42] R. J. Pugh, *Bubble and Foam Chemistry*, Cambridge University Press, Cambridge **2016**.
[43] R. Höhler, J. Seknagi, A. Kraynik, *Soft Matter* **2021**, *17*, 6995.
[44] Y. Y. C. Sang, PhD Thesis, Université Paris Diderot - Paris VII, **2009**.
[45] C. K. Kuo, P. X. Ma, *Biomaterials* **2001**, *22*, 511.
[46] L. Cascão Pereira, C. Johansson, H. Blanch, C. Radke, *Colloids Surf., A* **2001**, *186*, 103.
[47] Ó. Esteban, F. Marvá, J. C. Martínez-Antón, *Opt. Mater.* **2009**, *31*, 696.
[48] R. Kadri, G. Ben Messaoud, A. Tamayol, B. Aliakbarian, H. Y. Zhang, M. Hasan, L. Sánchez-González, E. Arab-Tehrany, *RSC Adv.* **2016**, *6*, 27879.
[49] D. Fang, Y. Liu, S. Jiang, J. Nie, G. Ma, *Carbohydr. Polym.* **2011**, *85*, 276.

 © 2022 The Authors. Macromolecular Rapid Communications published by Wiley-VCH GmbH

[50] J.-W. Lu, Y.-L. Zhu, Z.-X. Guo, P. Hu, J. Yu, *Polymer* **2006**, *47*, 8026.
[51] T. Okubo, K. Kobayashi, *J. Colloid Interface Sci.* **1998**, *205*, 433.
[52] H. Kaygusuz, G. A. Evingür, Ö. Pekcan, R. Von Klitzing, F. B. Erim, *Int. J. Biol. Macromol.* **2016**, *92*, 220.
[53] K. H. W. Rybinski, G. S. Alkyl, *Polyglycosides: Technology, Properties, and Applications*, Wiley-VCH, Weinheim **1997**.
[54] R. H. Colby, *Rheol. Acta* **2010**, *49*, 425.
[55] C. G. Lopez, R. H. Colby, P. Graham, J. T. Cabral, *Macromolecules* **2016**, *50*, 332.
[56] D. Y. C. Chan, E. Klaseboer, R. Manica, *Soft Matter* **2011**, *7*, 2235.
[57] D. Langevin, *Adv. Colloid Interface Sci.* **2020**, *275*, 102075.
[58] C. Üzüm, N. Kristen, R. Von Klitzing, *Curr. Opin. Colloid Interface Sci.* **2010**, *15*, 303.
[59] R. Von Klitzing, E. Thormann, T. Nylander, D. Langevin, C. Stubenrauch, *Adv. Colloid Interface Sci.* **2010**, *155*, 19.
[60] E. Chatzigiannakis, N. Jaensson, J. Vermant, *Curr. Opin. Colloid Interface Sci.* **2021**, *53*, 101441.
[61] E. Rio, A.-L. Biance, *ChemPhysChem* **2014**, *15*, 3692.
[62] K. P. Velikov, F. Durst, O. D. Velev, *Langmuir* **1998**, *14*, 1148.
[63] A. A. Sonin, A. Bonfillon, D. Langevin, *J. Colloid Interface Sci.* **1994**, *162*, 323.
[64] V. Chandran Suja, A. Kannan, B. Kubicka, A. Hadidi, G. G. Fuller, *Langmuir* **2020**, *36*, 11836.
[65] B. Kolarić, W. Jaeger, G. Hedicke, R. V. Klitzing, *J. Phys. Chem. B* **2003**, *107*, 8152.
[66] C. Stubenrauch, J. Schlarmann, R. Strey, *Phys. Chem. Chem. Phys.* **2002**, *4*, 4504.
[67] Y. Pocker, E. Green, *J. Am. Chem. Soc.* **1973**, *95*, 113.
[68] I. Fernández Farrés, I. T. Norton, *Food Hydrocolloids* **2014**, *40*, 76.
[69] S. T. Lee, N. S. Ramesh, in *Polymeric Foams: Mechanisms and Materials* (Eds: S. T. Lee, N. S. Ramesh) CRC Press, Boca Raton, FL **2004**.
[70] L. J. Evers, S. Y. Shulepov, G. Frens, *Phys. Rev. Lett.* **1997**, *79*, 4850.

 © 2022 The Authors. Macromolecular Rapid Communications published by Wiley-VCH GmbH